Smart Optode for 8-Wavelength Time-Gated Diffuse Optics

Laura Di Sieno, Giulia Maffeis, Alberto Dalla Mora, Edoardo Ferocino, Alberto Tosi, Enrico Conca, Alessandro Ruggeri, Simone Tisa, Alexander Flocke, Antonio Pifferi, and Paola Taroni

***Abstract*—We present the most compact (4 cm^3) time domain diffuse optical spectroscopy system, hosting 8 laser sources emitting at different wavelengths, a large area time-gated detector, and a time-to-digital converter. We tested the optode using standardized protocols, enlightening a high light harvesting capability and large penetration depth in detecting realistic optical inhomogeneities. We tested it also in vivo for the non-invasive assessment of blood parameters in a vascular occlusion test and for the detection of brain activation, demonstrating the optode capability to follow task-related hemodynamic changes even through a single measurement, with no need for averaging or filtering as instead needed with most available systems. The optode is thus a good candidate for next generation home-monitoring devices, thanks to its good performances, small dimension and potential low-cost.**

***Index Terms*—Hand-held diffuse optical probe, in vivo measurements of brain hemodynamics, time-gated diffuse optical spectroscopy.**

I. Introduction

TIME domain diffuse optics (TD-DO) is a powerful technique to non-invasively investigate diffusive media [1]. It relies on the injection of subnanosecond optical pulses in the medium, where they experience scattering and absorption events, and on the collection of the distribution of times-of-flight (DTOF) of photons that are re-emitted at a given distance (the so called "source-detector distance", SDD) from the injection point. The key advantages of the technique are: i) the capability to disentangle the contribution of the reduced scattering coefficient (μ_s', in the following named "scattering") from that of the absorption coefficient (μ_a), and ii) the encoding of the mean depth reached by photons in their travelling time. Those features make the TD-DO approach to be considered more informative than the continuous wave (CW) one [2], which however traditionally relies on a simpler and more compact instrumentation [3], [4]. Indeed, the main bottlenecks preventing the widespread use of TD-DO are the high costs of the required instrumentations (pulsed lasers, time-resolved single-photon detectors, and timing electronics) as well as their size and complexity. Moreover, as compared to CW systems, TD ones suffer from lower light harvesting capability, typically due to limited detector area and quantum efficiency. In the last years, several efforts were made to overcome those issues, leading to the development of compact sources, and timing electronics (namely time-to-digital converters, TDCs) [4]. In some cases, detector and timing electronics can be integrated in the same chip [5], [6], [7]. For what concerns the detector, in 2015 silicon photomultipliers (SiPMs) were successfully introduced in TD-DO [8]. Indeed, they are rugged and show high light harvesting capability thanks to their large area and to the possibility to be placed in contact with the sample, thus removing the need for optical fibers and the related losses. SiPMs have thus been chosen as detectors for different systems.

Overall, several steps towards the miniaturization of the TD-DO setup were taken, thus strongly reducing the overall system size, e.g., from a 2-channel book-like size device [8] to a wearable helmet with high-density of SDD pairs [9]. However, both of them show a relatively low diffused light harvesting capability (measured through the so-called "responsivity" parameters as dictated in the Basic Instrument Performance - BIP – Protocol [10]) in the order of about 10^{-8}–10^{-9} m^{2}sr. Moreover, due to the use of just two wavelengths, those systems are meant specifically for the assessment of blood parameters (volume and oxygenation). Furthermore, none of the above-mentioned compact systems exploits the so called "time-gated" approach, which is based on fast turning on and off the detector to selectively record only a fraction of the DTOF. This technique allows one to increase the dynamic range of the measurements and to improve the light harvesting of late arriving photons, which statistically probed a deep region of the turbid medium [11].

Manuscript received 29 March 2023; revised 27 September 2023; accepted 29 September 2023. Date of publication 2 October 2023; date of current version 15 December 2023. This work was supported by the European Union's Horizon 2020 research and innovation programme, under Grant 731877, SOLUS: Smart OpticaL and UltraSound diagnostics of breast cancer. *(Laura Di Sieno and Giulia Maffeis contributed equally to this work.) (Corresponding author: Alberto Dalla Mora.)*

This work involved human subjects or animals in its research. Approval of all ethical and experimental procedures and protocols was granted by the Ethical Committee of Politecnico di Milano under Application No. 13/2018, and performed in line with the Declaration of Helsinki.

Laura Di Sieno, Giulia Maffeis, Alberto Dalla Mora, Edoardo Ferocino, Antonio Pifferi, and Paola Taroni are with the Department of Physics, Politecnico di Milano, 20133 Milano, Italy (e-mail: laura.disieno@polimi.it; giulia.maffeis@polimi.it; alberto.dallamora@polimi.it; edoardo.ferocino@polimi.it; antonio.pifferi@polimi.it; paola.taroni@polimi.it).

Alberto Tosi and Enrico Conca are with the Department of Electronics, Information and Bioengineering, Politecnico di Milano, 20133 Milano, Italy (e-mail: alberto.tosi@polimi.it; enrico.conca@polimi.it).

Alessandro Ruggeri and Simone Tisa are with the Micro Photon Devices Srl, 39100 Bolzano, Italy (e-mail: alessandro.ruggeri@micro-photon-devices.com; simone.tisa@micro-photon-devices.com).

Alexander Flocke is with the iC-Haus GmbH, 55294 Bodenheim, Germany (e-mail: alexander.flocke@ichaus.de).

This article has supplementary material provided by the authors and color versions of one or more figures available at https://doi.org/10.1109/JSTQE.2023.3321436.

Digital Object Identifier 10.1109/JSTQE.2023.3321436

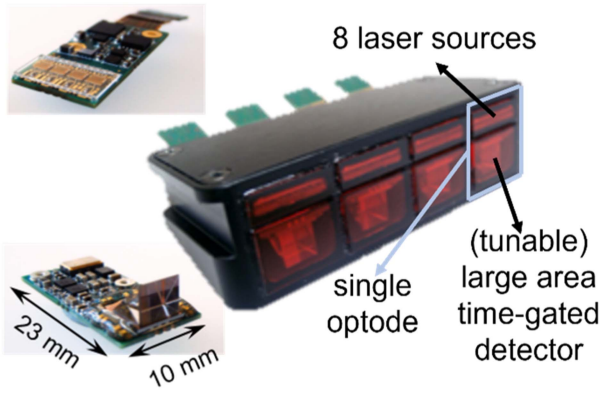

Fig. 1. Example of arrangement of 4 optodes. Each optode is composed of an array of 8 pulsed lasers at different wavelengths, a tunable large area time-gated SiPM and the integrated TDC.

The first SiPM (featuring up to 8.6 mm^2 active area) with time-gating capability was reported in 2020 and in the following year it was applied to TD-DO measurements showing a penetration depth of up to 3.75 cm [12], [13]. However, that detector was a stand-alone one, and still needed an external laser, thus making the whole system dimension far from being suitable for wearable devices.

In this work, we present the most compact 8-wavelength complete system (only few cm^3 for the whole smart optode, embedding laser sources, detector and timing electronics) capable of time-gated acquisitions. The miniaturized device was characterized using internationally shared protocols for TD-DO performance assessment, such as BIP, MEDPHOT and nEUROPt [10], [14], [15]. Moreover, proof-of-principle *in vivo* applications are reported for monitoring a vascular occlusion and for the detection of brain activation.

II. Optode Structure

Fig. 1 reports an example of an array of 4 optodes. Each optode is very compact (dimensions: $2.3 \times 1.2 \times 1.4\ cm^3$) and, as will be detailed in the following, it is composed of: i) an array of 8 pulsed laser sources at different wavelengths; ii) a tunable large area time-gated SiPM with integrated TDC; iii) the required control and power electronics. Each optode is an independent complete time domain multi-wavelength system. The arrangement of the optodes depicted in Fig. 1 is the one chosen for the SOLUS multi-modal probe where 2 cases, each one hosting 4 optodes, are placed on opposite sides of an ultrasound transducer. However, the mechanical mounting can be modified to arrange optodes in any number and desired geometry, making them suitable for a wide range of applications.

A. Laser Sources

Each optode embeds 8 laser diodes pulsed at subnanosecond level. To drive the lasers, a custom laser driver chip was developed. For each optode, four two-channel driver chips, designed in a 180 nm CMOS technology, are assembled in a chip-on-board technology to enable the most compact design possible. The chips have a specially developed communication structure that enables a higher-level processor unit to individually address, configure and operate the devices connected in chain. Each chip can individually drive two laser diodes with a peak current pulse of up to 1.2 A. The pulse widths can be set digitally from 100 ps to 5 ns in typical increments of 1 ps. Since the optode was developed for tissue spectroscopy within the SOLUS project (whose aim is to realize a multi-modal breast imaging system [16]), the nominal wavelengths of the laser drivers were chosen to match the spectra of typical constituents of human tissues (e.g., breast) [17]. Their nominal values are: 635, 670, 830, 915, 940, 980, 1030, and 1064 nm.

B. Large Area Time-Gated Detector, Optical Coupling, and Time-to-Digital Converter

The detector is a time-gated SiPM and it is composed of 1728 pixels, each one including 2 single-photon avalanche diodes (SPADs) with a square footprint with about 50 µm side and rounded corners. To increase the dynamic range of the overall acquisition, the active area of 32 pixels was reduced by circular pinholes. The SiPM was biased at 28.8 V, thus resulting in an excess bias (i.e., voltage above the breakdown of the device) of 3.3 V. More details on the detector architecture can be found in Ref. [12], whereas a complete characterization of SPADs fabricated in the same technology is reported in Ref. [18]. The detector lays on a printed circuit board that is mounted perpendicular to the optode window. Thus, a prism is used to convey the signal from the sample surface to the detector. The hypotenuse of the prism was metalized to improve the numerical aperture. A glass filter (Schott OG590) covers the surface of the detector to limit the contribution of the ambient light. The same filter covers also the laser window. The laser and the detector windows are physically separated to help reduce the spurious/direct light detection.

The timing electronics to record the DTOFs is based on a TDC embedded in the same chip, as widely described in Ref. [12]. Briefly, the TDC is based on a fully differential architecture and has a full-scale range of 9 ns. The conversions results are stored in 128 counters (12-bit each one) to build the DTOF. The typical resolution is about 77 ps and a dithering correction is applied to reduce non-linearity.

C. Optode and Control Electronics

Inside the optode, the 8 laser diodes and 4 laser driver Integrated Circuits (ICs) are hosted on a printed circuit board, whilst the detector is on a separate one. The boards are mounted on opposite sides of the optode chassis and connected via a small form factor connector. Other key onboard components are: i) a crystal oscillator, used as time reference for the TDC; ii) a few voltage regulators and voltage/current monitoring ICs; iii) a discrete logic gate to handle a safety interlock protection; iv) a 16-bit microcontroller. The last acts as a bridge between the optode active components and an external master microcontroller, able to control many optodes. The optode microcontroller directly manages the laser driver and detector operations, acquires data from the detectors, and relays them upstream for processing

TABLE I
SPECTRUM AND POWER VALUES OF LASERS HOSTED IN OPTODE 1 AND 2 (RESPECTIVELY, OPT 1 AND OPT 2) AT DIFFERENT WAVELENGTHS (λ)

Nominal λ (nm)	Spectrum (nm)				Average power (mW)	
	Central λ		FWHM			
	Opt 1	Opt 2	Opt 1	Opt 2	Opt 1	Opt 2
635	646	646	2.6	2.5	1.1	1.8
670	681	680	3.1	3.1	3.5	2.5
830	838	837	11.3	11.5	1.3	1.3
915	916	914	8.7	10.0	6.5	5.2
940	938	937	14.7	14.0	4.0	4.8
980	979	978	7.8	7.2	3.0	1.5
1030	1029	1029	18.2	18.2	3.7	3.4
1064	1053	1054	23.9	23.4	4.8	4.7

and/or storage. On the other hand, the higher-level control electronics takes care of supply generation for all optode components starting from a single external DC rail, distributes the common synchronization signal for lasers and detectors, and provides data connectivity toward the external world. A block diagram of the main components and the signal involved is reported in the Supplement 1 (Fig. S1).

III. OPTODE PERFORMANCES

The optode performances were assessed using well-shared protocols, namely BIP, MEDPHOT and nEUROPt [10], [14], [15]. The first is connected to the basic performances of the device without any diffusive medium, the second assesses the capability to retrieve the optical properties of a homogeneous medium, while the last deals with the capability to detect an optical perturbation.

To recover optical properties and/or detect optical perturbations, the literature suggests using a SDD in the order of few centimeters. For that reason, we used a single optode for both sources and detector with almost null SDD (in the following, optode 1) plus the laser sources of another optode (optode 2) whose distance from the detector of optode 1 was about 2.6 cm.

Finally, the use of the optode for a proof-of-principle *in vivo* application (i.e., detection of brain activation) is shown.

For all measurements, to avoid the heating and degradation of the detector performance (e.g., increase in the dark count rate - DCR), the overall number of pixels in the "*on*" state was limited setting an active area of about 5.3 mm^2.

A. Basic Performances: Laser Characterization, Responsivity, Instrument Response Function Shape

The characterization of the laser sources in terms of spectrum (central wavelength and full-width at half maximum –FWHM– as well as average power), as dictated by the BIP protocol [10], is reported in Table I. The central wavelength is always close to the nominal one with no dependence of the discrepancy on wavelength, while the spectral width increases with wavelength, from 3 to 24 nm. The output power of the lasers is comparable with state-of-the-art clinical systems [19], being always above 1 mW and in some cases exceeding 5 mW.

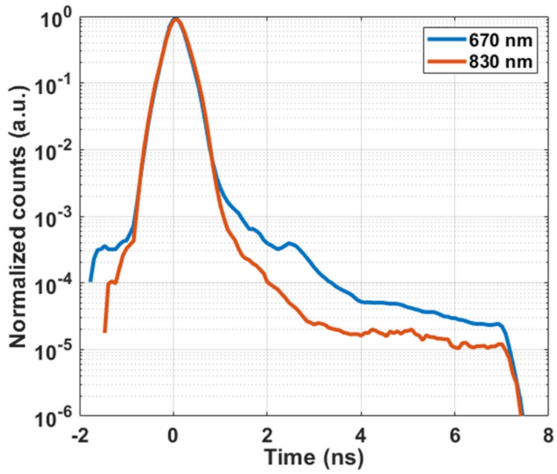

Fig. 2. Reconstructed IRF of the optode 1 at two wavelengths (670 and 830 nm, blue and orange curve, respectively).

Due to the geometry of the optode, it is not possible to measure the diffuse responsivity (i.e., the photon counting efficiency from a reference diffuse source) using the 8 laser diodes. Thus, we made use of an external dual wavelength picosecond laser (PDL 828 Sepia II driver coupled to LDH-P-C-670M and LDH-P-C-830M laser heads, all from Picoquant GmbH, Germany). For the optode, the responsivity was computed to be $1.8 \cdot 10^{-6}$ and $5.1 \cdot 10^{-7}$ m^2sr (at 670 and 830 nm, respectively). Despite the achieved level of miniaturization, those values are among the highest ever reported in the field. Further, they are slightly higher than those obtained with the gated SiPM reported in Ref. [13]. That could be ascribed to the improved optical coupling between the detector and the probe surface and to slightly different detector conditions (i.e., excess bias voltage, temperature, etc.).

The instrument response function (IRF) was acquired by slicing the DTOF in different fractions obtained moving the temporal window of the detector (namely hardware delays) and then reconstructed for all wavelengths as follows. Due to the geometry of the optode, a black PVC plate with a thin groove was used to guide the light from the lasers to the detector. Laser wavelengths were scanned sequentially. For a given laser source, the hardware delay was moved (in steps of nearly 300 ps, up to an overall delay of around 3.9 ns) to acquire different portions of the DTOF, adjusting the number of pixels turned on to keep the count-rate constant. The different hardware delays were then rescaled by the area corresponding to the number of pixels on and then only a fraction of about 350 ps was used [20].

Two examples of reconstructed IRFs (at 670 and 830 nm) are reported in Fig. 2. The IRF can be characterized through its temporal width (expressed as FWHM) computed on the first hardware delay and its dynamic range. For both wavelengths, the IRF has width of about 390 ps FWHM and dynamic range of about 5 decades. The difference in the slow decay tail can be ascribed to the different contribution of the so called "memory effect" at different wavelengths [11]. Similar results were achieved also for the other wavelengths and are summarized in terms of FWHM and dynamic range (calculated with reference to the asymptotic value of the slow diffusion tail, after normalizing

TABLE II
CHARACTERISTICS OF THE IRF OF OPTODE 1 AT THE DIFFERENT WAVELENGTHS (λ)

Nominal λ (nm)	FWHM (ps)	Dynamic range (compared to peak)
635	435	3.5 E-5
670	390	2.5 E-5
830	392	1.0 E-5
915	334	1.2 E-5
940	382	1.0 E-5
980	410	2.0 E-5
1030	424	2.0 E-5
1064	443	2.0 E-5

the IRF peak to one) in Table II. For what concerns the 670 nm IRF, a slight peak (almost 4 decades below the peak) at 2.5 ns can be distinguished. It is most probably due to an artifact in the reconstruction caused by the relatively loose step of the delayer (300 ps). This value, however, was found to be the best compromise between a sufficiently smooth reconstruction and the duration of the whole acquisition.

B. Capability to Retrieve Optical Properties of Homogeneous Media

Thanks to the presence of 8 wavelengths, the optode can be used as a miniaturized spectroscopy system. The suitability of the optode for TD diffuse optical spectroscopy is tested using the well-accepted MEDPHOT protocol [14]. It is based on a kit of 32 phantoms, combining 8 nominal absorption values (0 to 0.35 cm^{-1} in steps of 0.05 cm^{-1}, labelled with numbers 1 to 8) with 4 scattering coefficients (5 to 20 cm^{-1} in steps of 5 cm^{-1}, labelled with letters A to D). More details about the nominal properties of the phantoms can be found in Supplement 1 (Paragraph 2).

The linearity test foreseen in the MEDPHOT protocol was exploited to enlighten the capability of the system to properly recover optical properties. To that purpose the reconstructed curve was recorded moving the hardware delay in steps of 200 ps up to an overall delay of around 3.8 ns. For each wavelength, 340 repetitions (each one acquired with an integration time of 5 ms) were summed to have an actual acquisition time of 1.7 s. To recover the optical properties of the homogeneous medium, curves were fitted to an analytical model obtained under the Diffusion Approximation describing the photon transport in an infinite diffusive medium [21]. To reach convergence, the reduced χ^2 was minimized using a Levenberg-Marquardt routine [22]. The finite response of the optode was taken into account by convolving the IRF to the analytical model. The curves were fitted from 50% of the peak on the rising edge down to 0.001% of the peak on the falling edge of the acquired waveform.

Figs. 3 and 4 report the results of the linearity test at 670 and 830 nm. Two (top left and bottom right) graphs show the linearity in the retrieval of μ_a and μ_s' (i.e., the capability of the system to follow linear variations of μ_a and μ_s'), while the other two enlighten the coupling between the measured absorption

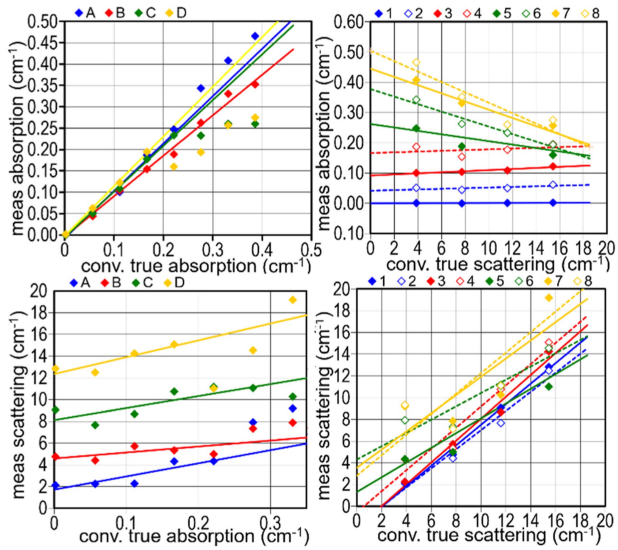

Fig. 3. Measured absorption and scattering values (top and bottom respectively) as a function of the conventionally true absorption and scattering (left and right, respectively) at 670 nm.

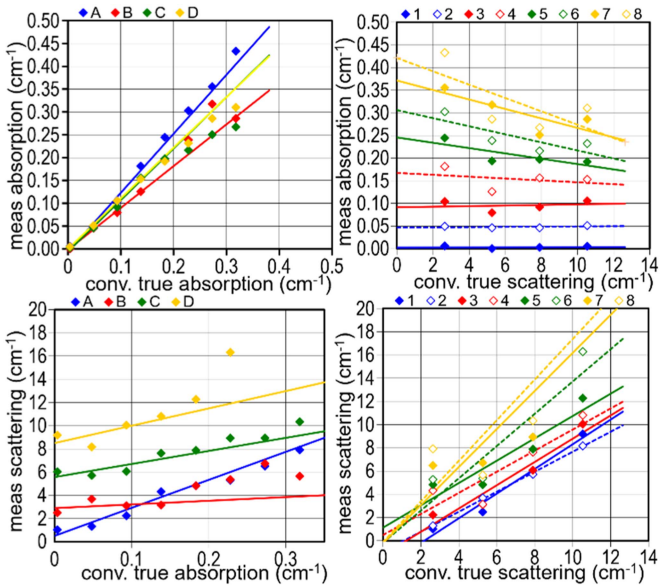

Fig. 4. Measured absorption and scattering values (top and bottom respectively) as a function of the conventionally true absorption and scattering (left and right, respectively) at 830 nm.

and the conventionally true reduced scattering of the phantom (i.e., scattering-to-absorption coupling, top right graph) and vice versa (i.e., absorption-to-scattering coupling, bottom left graph). For the measured absorption coefficient, the optode is capable to follow linear variations of μ_a. Only at 670 nm, with the highest scattering series (C and D), high absorption values cannot be properly retrieved. On the other hand, for phantoms with low absorption (up to series 5 for 670 nm and 6 for 830 nm) the retrieved μ_a is completely independent of the phantom scattering.

The retrieval of the scattering is more delicate, and some issues are enlightened by the MEDPHOT protocol. Indeed, the linearity in the retrieval of the scattering coefficient is sufficient

for phantoms with lower absorption (up to series 5), while a substantial coupling between the recovered scattering and the conventionally true absorption can be observed. Similar conclusions can be drawn for the other wavelengths (whose results are reported in the Supplemental 1, Fig. S2-S7).

The MEDPHOT protocol highlights a general issue in the optode performance to properly retrieve the reduced scattering. At hardware level, different causes can be postulated, leading to possible ways of improvements, namely: a) the relatively large IRF FWHM causing a higher indeterminacy in the location of scattering-related peak position, mostly related to the not-identical temporal response of activated pixels depending on pixel position over the chip [12]; b) the subtle effects of the glass windows opening a tiny light-guiding shortcut; c) the possible non-time invariancy of the gating mechanism due to the non-perfectly square shape of the gating pulse [12], [23]. Potential improvements can be proposed. First, sectioning of the glass window could reduce the light-guiding effect (b), while an optimized distribution of the bias across the chip could reduce voltage bouncing affecting the gating mechanism (c). Furthermore, the improvement of the breakdown voltage uniformity over the time-gated SiPM chip (an issue extensively reported in [12]) can minimize the effect of (a). Issues (a) and (c) undermine the key assumptions of the convolution theorem. A machine learning approach, trained on a wide combination of optical properties derived from highly characterized Intralipid and ink solutions [24], could be exploited at post-processing to better account for the distortion of the detector beyond the pure convolution with the IRF and help also in curing the effects of items (a) and (c).

At any rate, tissue spectroscopy mostly relies on absorption, which is used to compute the tissue composition and its variations (e.g., spatial heterogeneity or time dynamics). Therefore, the absorption linearity and the effect of scattering on the absorption retrieval are the two most important parameters to consider, and in our case they show the best performance.

C. Penetration Depth Inside Heterogeneous Media

To assess the capability of the optode to detect an optical inhomogeneity buried in depth within a (homogeneous) medium (e.g., to detect a tumor in the breast or the task-related activation of the brain) we adopt two figures of merit defined in the nEUROPt protocol: the contrast (C) and the contrast-to-noise-ratio (CNR) [15]. The former is the percentage change in the number of counts between the homogeneous state (e.g., healthy breast or rest state of the brain during exercise) with respect to the heterogeneous one (e.g., breast with a tumor or brain activation during a task). The latter is an index of the robustness of the contrast with respect to the intrinsic fluctuations of the measurement (calculated as the standard deviation of the number of counts in the homogeneous case). Both C and CNR can be computed in so called "time gates" (i.e., given fractions of the acquired DTOF).

Due to the possibility to use lasers from two different optodes, both the almost null SDD (laser and detector of optode 1) and the more "standard" 2.6 cm SDD (laser of optode 2, detector of optode 1) approaches have been explored.

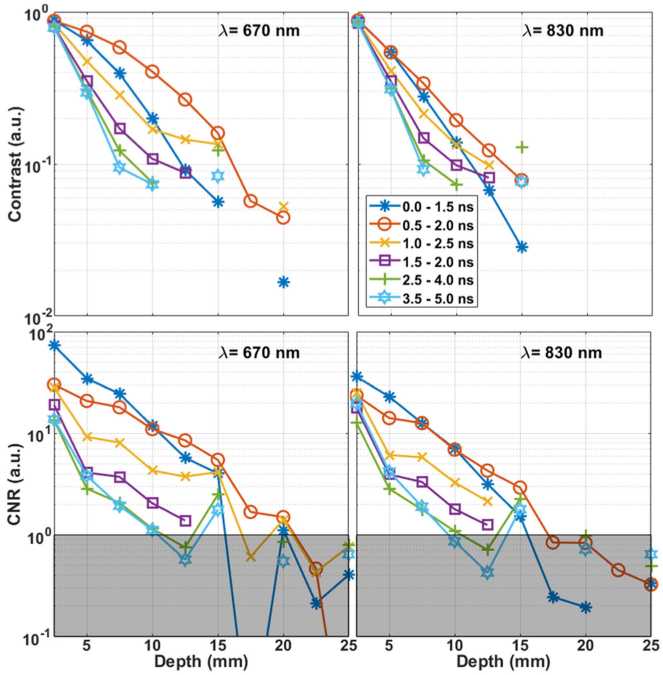

Fig. 5. Contrast (top) and CNR (bottom) obtained with almost null SDD, for 670 and 830 nm (left and right, respectively). Colors and symbols represent different time gates (referred to the IRF peak) used for analysis.

The contrast measurements were made using a water-based phantom where Intralipid and Indian Ink were added in calibrated quantities to give the desired scattering and absorption properties [24]. An optical perturbation ($\Delta\mu_a$) was induced by the 100 mm^3 totally absorbing cylinder (with diameter = height = 5 mm) [25]. The optical properties of the phantom and of the optical perturbation depend on the laser wavelength (see Table S3 in the Supplemental 1).

The liquid phantom was hosted in a black tank featuring a 50-μm thick Mylar window. To avoid direct light, the optode was placed in contact with the Mylar window through a thin layer of diffusive ultrasound gel [26]. To test the depth sensitivity of the system, the center of the perturbation was moved in depth by a motorized slit (step precision: 10 μm) from 2.5 mm to 45 mm with respect to the optode surface. Once the perturbation had reached a given depth, all lasers shone sequentially. At each wavelength, data were acquired with several hardware delays (the same for all wavelengths). An integration time of 15 ms per hardware delay was chosen, and the measurement cycle was repeated 67 times to reach the actual 1 s acquisition, as defined by nEUROPt protocol. After signal acquisition, for each hardware delay an acquisition was made with all lasers off to allow background subtraction. This procedure was followed in post-processing after the counting-loss correction due to the dead-time of the time-to-digital converter (TDC) [27] and before the calculation of the figures of merits. The contrast was computed using a time gate (one for each hardware delay) of 1.5 ns width whose position with respect to the IRF peak was delayed by the value reported in the legend of the corresponding figures (Figs. 5 and 6, and Figs. S8–S11 in Supplement 1).

Figs. 5 and 6 report the results obtained for both 670 and 830 nm (left and right column) at almost null and 2.6 cm SDD,

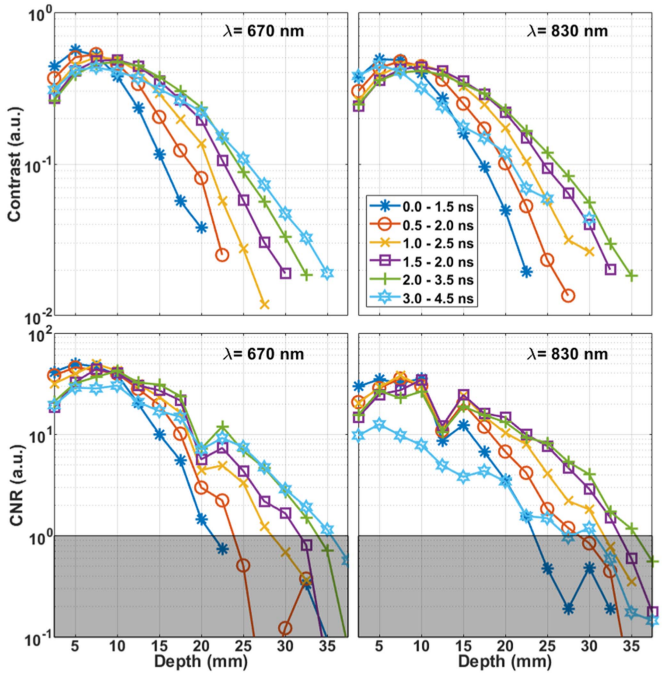

Fig. 6. Contrast (top) and CNR (bottom) obtained with 2.6 cm SDD, for 670 and 830 nm (left and right, respectively). Colors and symbols represent different time gates (referred to the IRF peak) used for analysis.

respectively. At 670 and 830 nm, the absorption coefficient is nearly constant (0.10 and 0.11 cm^{-1}, respectively) and the scattering decreases with wavelength (10.50 and 8.00 cm^{-1}, respectively), while the optical perturbation increases (0.16 and 0.18 cm^{-1}, respectively, over 1 cm^3).

The use of almost null SDD is clearly limiting the maximum penetration depth (considered as the point where $C > 1\%$ with $CNR > 1$) to 2.0 cm, while the use of a larger SDD allows one to reach a depth of 3.5 cm. Indeed, as demonstrated in other works, while theoretically convenient [28], in practice the use of an almost null SDD, results in worst performances due to the non-idealities of the system (e.g., memory effect, finite shape of the IRF etc. [29]).

The contrast and the CNR for all wavelengths can be found in Supplement 1. For longer wavelengths, the penetration depth decreases (due to the complex interplay between spectrally dependent optical parameters of phantom/perturbation and to the quantum efficiency of the detector) ranging from 1.75 (at 980 nm: worst case, with high absorption of the homogeneous medium due to the water peak) and 3.25 cm (at 915 nm).

D. In Vivo Proof-of-Concept

To test the capability of the system to properly distinguish variations of oxy- and deoxyhemoglobin (HbO_2 and HHb, respectively), we performed measurements: i) to track an arterial occlusion, and ii) to detect brain activation during a finger-tapping exercise.

To distinguish between HbO_2 and HHb, only two wavelengths (670 and 830 nm, typical values for functional near infrared spectroscopy) are needed [3].

Written informed consent was given by participants. The protocols were approved by the Ethical Committee of Politecnico di Milano and conducted in agreement with the Declaration of Helsinki. A photograph, reporting the application scene in both applications (arterial occlusion and detection of brain activation), is reported in the Supplement 1 (Fig. S12).

1) Arterial Occlusion: The arterial occlusion was induced by a sphygmomanometer cuff put on the subject's forearm. The protocol consisted in 60 s of baseline (i.e., no alteration of blood flow) followed by a 240 s of occlusion and then a recovery phase of 180 s. To induce an arterial occlusion (i.e., complete blockage of both venous and arterial blood circulation), the pressure applied to the cuff had a value (i.e., 250 mmHg) well above the subject's systolic pressure.

Due to the massive and homogeneous (i.e., not localized in depth as instead in the case of brain activation) change in hemodynamics induced by the arterial occlusion, we used only one hardware delay equivalent to the free-running mode (i.e., the detector was turned on before the first re-emitted photon was collected and turned off when the DTOF was extinguished).

For each wavelength, a time gate of 1 ns width was opened 500 ps after the IRF peak. For both wavelengths we computed a quantity proportional to the variation in the absorption coefficient ($k\,\Delta\mu_a$) as stated in (1):

$$k\Delta\mu_a = -\ln\frac{N\,(t)}{N_0\,(t)} \tag{1}$$

where k is a constant, $N(t)$ is the number of counts in the time gate for each time instant t, while $N_0(t)$ was computed as the average value of photons detected within the rest phase.

Then, considering the extinction coefficient of HbO_2 and HHb and applying the Beer's law for mixtures, it is possible to compute the relative variation in concentration of the two chromophores.

Fig. 7 reports the variation in oxy- and deoxyhemoglobin during the arterial occlusion task. A clear task-related change in HbO_2 and HHb can be observed during the occlusion phase (60 s to 300 s). Indeed, due to the blockage of the blood circulation, HbO_2 cannot be supplied. Thus, upon its conversion into HHb, its concentration decreases, while the HHb one correspondingly increases, leaving the total hemoglobin ($HbO_2 + HHb$) constant. Once the occlusion is released, the wash out of the HHb and a large inflow of HbO_2 can be observed before return to the baseline. The recorded trends of HHb and HbO_2 are in line with state-of-the-art measurements, thus validating the capability of the optode to properly detect variations in chromophore concentrations. The lower signal-to-noise ratio in the HbO_2 can be ascribed to the lower photon harvesting capability of the system at 830 nm (more sensitive to the oxy-hemoglobin), combined with lower laser power at this wavelength. Indeed, if compared to the 670 nm, at this wavelength the laser power is 2 times lower (see Table I) and the responsivity is almost 4 times smaller (as reported in Section III-A). This causes an overall reduction of the signal of almost a decade which may be reflected in the higher noise in the HbO_2

2) Detection of Brain Activation: The optode was tested in the detection of brain activation during a finger-tapping exercise.

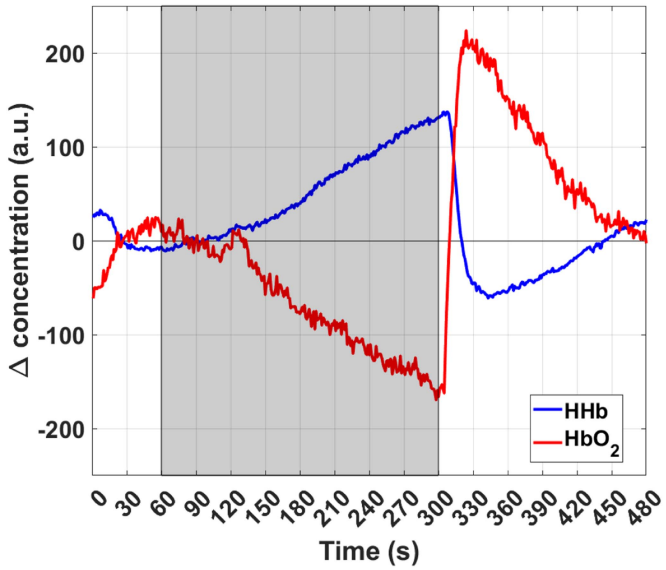

Fig. 7. Variation in concentration of oxy- (red line) and deoxygenated (blue line) hemoglobin during the arterial occlusion protocol. The gray shadowed region corresponds to the period in which the blood circulation was blocked ("occlusion phase").

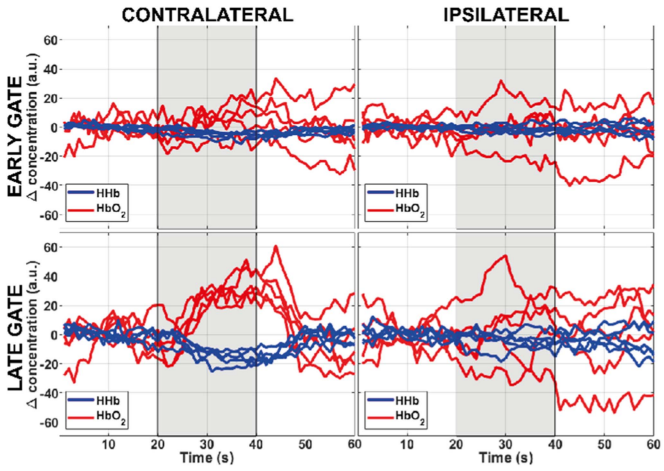

Fig. 8. Variation in HHb and HbO_2 concentrations (blue and red lines, respectively) obtained for contralateral and ipsilateral task (left and right column) using an early and a late gate (top and bottom, respectively).

As depicted in Paragraph III.C, the best penetration depth is achieved using a large SDD, thus as sources we used the lasers of optode 2. The optode was centered on the motor cortex (C3 position) of the subject's head and the two wavelengths shone sequentially.

For each wavelength, two hardware delays were chosen: one equivalent to the free-running mode and another one delayed up to when 2 Mcps can be reached. A gated analysis was then done: the hardware delay equivalent to the free-running was used for the early gate, while the delayed one for the calculation of late gate, focusing on the tail of the DTOF.

The task (repeated with left and right hand, i.e., ipsilateral and contralateral task, respectively) consisted of 20 s of rest, 20 s of finger tapping, and 20 s of recovery. It was repeated 5 times. The variation in HbO_2 and HHb, computed as explained in the previous Sect. and expressed in arbitrary units, was computed using the resting state as a reference for each repetition of the task.

Fig. 8 reports the estimated variation in HHb and HbO_2 concentrations (blue and red lines, respectively). Provided that a late gate (i.e., 3 ns from the IRF peak, obtained setting the hardware delay of about 3.2 ns) is used, the task-related fingerprint of brain activation (i.e., increase in HbO_2 and decrease in the HHb) can be seen in each repetition, while usually in functional near infrared spectroscopy applications, a folding average among repetitions is needed to get a robust and detectable signal. The average among repetitions is displayed in Fig. S13 of Supplement 1.

The advantage of a time-gated measurement with respect to a standard (i.e., free-running) one can be enlightened comparing the results obtained using an early gate (i.e., 1 ns from the IRF peak), where no activation can be detected. The larger visibility of the brain activation using a late gate is expected since the area of interest is placed around 1.5-2 cm deep, thus the detection of late photons is needed to retrieve information about cortex oxygenation.

The ipsilateral task, for both early and late time gates, shows no task-related changes, as expected.

IV. Conclusion And Future Perspectives

To the best of our knowledge, the presented optode is the most compact complete device for time domain diffuse optical spectroscopy. Indeed, in 4 cm^3 it hosts 8 sources, a large-area time-gated detector and the TDC. Since it is built using commercially available components and ASICs fabricated in standard CMOS processes, and thanks to its small size, it is foreseeable that unit cost could easily scale down with volume production. Its performances assessed, following well shared protocols, show that the optode features one of the best light harvesting capabilities (thanks to its large active area) and a large dynamic range (5 or more decades, thanks to the time gating capability). The IRF shape, despite being slightly larger than state-of-the-art clinical systems, is not affecting the depth penetration capability: the optode proved capable to detect a perturbation buried up to 3.5 cm in depth, which is even better than state-of-the-art bulky clinical systems (usually limited to no more than 3.0 cm).

The large responsivity coupled to the time gating capability allows one to obtain striking results in terms of brain activation detection: using the optode, a finger tapping exercise can be distinguished even in a single acquisition, with no need for filtering or averaging over repeated measurements. Moreover, as clearly enlightened for the *in vivo* brain detection, the use of the hardware delay gives large flexibility since it permits to tune the measurement conditions depending on the specific use.

For what concerns spectroscopy applications, the optode shows limitations in the accurate recovering of the scattering coefficient of homogeneous media, while acceptable results are obtained for the absorption one. However, in several applications (e.g., brain imaging and optical mammography) the scattering is supposed to be constant while variations of the absorption

coefficient need to be linearly detected. More in general, even if the scattering changes, our optode fails in correctly assessing it, but the absorption estimate is fairly unaffected. For all those applications, the optode represents a valid alternative for future low-cost instruments for home care monitoring or for other industrial applications (e.g., non-destructive assessment of fruit quality or ripeness on the field). Moreover, the arrangement of multiple optodes can be a compact and easy-to-use option for the development of tomography systems for medical imaging. As an example, the SOLUS probe, which is based on 8 optodes, is currently being tested in a clinical study on the non-invasive differentiation of malignant and benign breast lesions relying on multi-wavelength diffuse optical tomography combined with ultrasound imaging techniques.

References

[1] B. Chance, *Photon Migration in Tissues*. New York, NY, USA: Plenum Press, 1989, doi: 10.1007/978-1-4757-6178-8.

[2] T. Durduran, R. Choe, W. B. Baker, and A. G. Yodh, "Diffuse optics for tissue monitoring and tomography," *Rep. Prog. Phys.*, vol. 73, no. 7, Jul. 2010, Art. no. 076701, doi: 10.1088/0034-4885/73/7/076701.

[3] F. Scholkmann et al., "A review on continuous wave functional near-infrared spectroscopy and imaging instrumentation and methodology," *Neuroimage*, vol. 85, pp. 6–27, 2014, doi: 10.1016/j.neuroimage.2013.05.004.

[4] A. Pifferi et al., "New frontiers in time-domain diffuse optics, a review," *J. Biomed. Opt.*, vol. 21, no. 9, Jun. 2016, Art. no. 091310, doi: 10.1117/1.JBO.21.9.091310.

[5] C. Niclass, C. Favi, T. Kluter, M. Gersbach, and E. Charbon, "A 128 × 128 single-photon image sensor with column-level 10-bit time-to-digital converter array," *IEEE J. Solid-State Circuits*, vol. 43, no. 12, pp. 2977–2989, Dec. 2008, doi: 10.1109/JSSC.2008.2006445.

[6] N. A. W. Dutton et al., "A time-correlated single-photon-counting sensor with 14GS/S histogramming time-to-digital converter," in *Proc. Dig. Tech. Papers IEEE Int. Solid State Circuits Conf.*, 2015, pp. 204–205, doi: 10.1109/ISSCC.2015.7062997.

[7] N. Krstajić et al., "0.5 billion events per second time correlated single photon counting using CMOS SPAD arrays," *Opt. Lett.*, vol. 40, no. 18, pp. 4305–4308, 2015, doi: 10.1364/ol.40.004305.

[8] A. Dalla Mora et al., "The SiPM revolution in time-domain diffuse optics," *Nucl. Instrum. Methods Phys. Res. A*, vol. 978, Oct. 2020, Art. no. 164411, doi: 10.1016/j.nima.2020.164411.

[9] H. Y. Ban et al., "Kernel flow: A high channel count scalable time-domain functional near-infrared spectroscopy system," *Proc. SPIE*, vol. 27, no. 07, pp. 1–19, 2022, doi: 10.1117/1.jbo.27.7.074710.

[10] H. Wabnitz et al., "Performance assessment of time-domain optical brain imagers, part 1: Basic instrumental performance protocol," *J. Biomed. Opt.*, vol. 19, no. 8, Aug. 2014, Art. no. 086010, doi: 10.1117/1.JBO.19.8.086010.

[11] A. Dalla Mora, L. Di Sieno, R. Re, A. Pifferi, and D. Contini, "Time-gated single-photon detection in time-domain diffuse optics: A review," *Appl. Sci.*, vol. 10, no. 3, Feb. 2020, Art. no. 1101, doi: 10.3390/app10031101.

[12] E. Conca et al., "Large-area, fast-gated digital SiPM with integrated TDC for portable and wearable time-domain NIRS," *IEEE J. Solid-State Circuits*, vol. 55, no. 11, pp. 3097–3111, Nov. 2020, doi: 10.1109/JSSC.2020.3006442.

[13] L. Di Sieno et al., "Time-domain diffuse optics with 8.6 mm^2 fast-gated SiPM for extreme light harvesting," *Opt. Lett.*, vol. 46, no. 2, pp. 424–427, 2021, doi: 10.1364/OL.413577.

[14] A. Pifferi et al., "Performance assessment of photon migration instruments: The MEDPHOT protocol," *Appl. Opt.*, vol. 44, no. 11, pp. 2104–2114, Apr. 2005, doi: 10.1364/AO.44.002104.

[15] H. Wabnitz et al., "Performance assessment of time-domain optical brain imagers, part 2: NEUROPt protocol," *J. Biomed. Opt.*, vol. 19, no. 8, Aug. 2014, Art. no. 086012, doi: 10.1117/1.JBO.19.8.086012.

[16] "SOLUS - Smart optical and ultrasound diagnostics of breast cancer," H2020 Proj. grant No. 731877. Accessed: 2023. [Online]. Available: http://www.solus-project.eu/

[17] S. L. Jacques, "Optical properties of biological tissues: A review," *Phys Med Biol*, vol. 58, no. 11, pp. R37–R61, 2013, doi: 10.1088/0031-9155/58/11/R37.

[18] M. Buttafava et al., "SPAD-based asynchronous-readout array detectors for image-scanning microscopy," *Optica*, vol. 7, no. 7, pp. 755–765, Jul. 2020, doi: 10.1364/OPTICA.391726.

[19] R. J. Cooper et al., "MONSTIR II: A 32-channel, multispectral, time-resolved optical tomography system for neonatal brain imaging," *Rev. Sci. Instrum.*, vol. 85, no. 5, 2014, Art. no. 053105, doi: 10.1063/1.4875593.

[20] A. Tosi et al., "Fast-gated single-photon counting technique widens dynamic range and speeds up acquisition time in time-resolved measurements," *Opt. Exp.*, vol. 19, no. 11, pp. 10735–10746, May 2011, doi: 10.1364/OE.19.010735.

[21] D. Contini, F. Martelli, and G. Zaccanti, "Photon migration through a turbid slab described by a model based on diffusion approximation I theory," *Appl. Opt.*, vol. 36, pp. 4587–4599, 1997, doi: 10.1364/AO.36.004587.

[22] W. H. Press, S. A. Teukolsky, W. T. Vetterling, and B. P. Flannery, *Numerical Recipes in C*, Cambridge Univ. Press, 1988.

[23] D. Contini et al., "Effects of time-gated detection in diffuse optical imaging at short source-detector separation," *J. Phys. D Appl. Phys.*, vol. 48, no. 4, Feb. 2015, Art. no. 045401, doi: 10.1088/0022-3727/48/4/045401.

[24] L. Spinelli et al., "Determination of reference values for optical properties of liquid phantoms based on Intralipid and India ink," *Biomed. Opt. Exp.*, vol. 5, no. 7, pp. 2037–2053, 2014, doi: 10.1364/BOE.5.002037.

[25] F. Martelli et al., "Phantoms for diffuse optical imaging based on totally absorbing objects, part 1: Basic concepts," *Proc. SPIE*, vol. 18, no. 6, Jan. 2013, Art. no. 066014, doi: 10.1117/1.JBO.18.6.066014.

[26] L. Di Sieno et al., "Systematic study of the effect of ultrasound gel on the performances of time-domain diffuse optics and diffuse correlation spectroscopy," *Biomed. Opt. Exp.*, vol. 10, no. 8, pp. 3899–3915, 2019, doi: 10.1364/BOE.10.003899.

[27] W. Becker, *The BH TCSPC Handbook*, 6th ed. Berlin, Germany: Becker & Hickl GmbH, 2014.

[28] A. Pifferi et al., "Time-resolved diffuse reflectance using small source-detector separation and fast single-photon gating," *Phys. Rev. Lett.*, vol. 100, no. 13, Mar. 2008, Art. no. 138101, doi: 10.1103/PhysRevLett.100.138101.

[29] A. Behera, L. Di Sieno, A. Pifferi, F. Martelli, and A. D. Mora, "Instrumental, optical and geometrical parameters affecting time-gated diffuse optical measurements: A systematic study," *Biomed. Opt. Exp.*, vol. 9, no. 11, pp. 5524–5542, Nov. 2018, doi: 10.1364/BOE.9.005524.

Laura Di Sieno was born in Varese, Italy, in 1987. She received the master's degree in electronics engineering and the Ph.D. degree in physics from the Politecnico di Milano, Milan, Italy, in 2011 and 2015, respectively.

She is currently an Assistant Professor with the Department of Physics, Politecnico di Milano. She has authored more than 80 papers in international peer-reviewed journals and conference proceedings.

Dr. Di Sieno's activity is mainly focused on the study and application of a new approach and instrumentation for time-domain optical spectroscopy of highly scattering media using single-photon detectors.

Giulia Maffeis received the master's degree in engineering physics from the Politecnico di Milano, Milan, Italy, where she is currently working toward the Ph.D. degree in physics. Her research interests include photon migration in turbid media, non-invasive near-infrared diffuse spectroscopy, and imaging with time-resolved systems. She focuses on technologies and data analysis methods for diffuse optical mammography.

Alberto Dalla Mora was born in Fiorenzuola d'Arda, Italy, in 1981. He received the M.Sc. degree in electronics engineering and the Ph.D. degree in information and communication technology from the Politecnico di Milano, Milan, Italy, in 2006 and 2010, respectively.

He is currently an Associate Professor with the Physics Department, Politecnico di Milano. He has authored about 190 papers in international peer-reviewed journals and conference proceedings.

His research interests mainly include development of innovative time-resolved diffuse optics techniques and instrumentation for biomedical applications.

Edoardo Ferocino received the M.Sc. Physics Engineering and the Ph.D. degrees in physics from the Politecnico di Milano, Milan, Italy, in 2016 and 2020, respectively. He worked on diffuse optical breast imaging, focusing on the implementation of software and the development of instrumentations to perform time-resolved measurements. His research focuses on the coding and test of data analysis models based on perturbative approaches.

Alberto Tosi was born in Borgomanero, Italy, in 1975. He received the master's degree in electronics engineering and the Ph.D. degree in information technology engineering from the Politecnico di Milano, Milan, Italy, in 2001 and 2005, respectively. From 2006 to 2014, he was an Assistant Professor. Since 2014, he has been an Associate Professor of electronics with the Politecnico di Milano. In 2004, he was a Student with the IBM T. J. Watson Research Center, Yorktown Heights, NY, working on optical testing of CMOS circuits. He currently works on silicon and InGaAs/InP single-photon avalanche diodes (SPADs). His research interests include arrays of silicon SPADs for 2-D and 3-D applications and time-correlated single-photon counting electronics.

Enrico Conca was born in Cremona, Italy, in 1992. He received the master's degree (*cum laude*) in electronics engineering and the Ph.D. degree in information technology from the Politecnico di Milano, Milan, Italy, in 2016 and 2019, respetively. He is currently a Postdoctoral Researcher with the Department of Electronics, Information and Bioengineering, Politecnico di Milano. His research interests focuses on the design and development of time-gated single photon counting circuits in CMOS and BCD technologies.

Alessandro Ruggeri was born in Alzano Lombardo, Italy, in 1987. He received the master's degree in electronics engineering and the Ph.D. degree in information technology from the Politecnico di Milano, Milan, Italy, in 2012 and 2015, respectively. As student, he worked on optical testing of VLSI circuits with IBM T. J. Watson Research Center, Yorktown Heights, NY, USA. After a few years as a R&D designer, he is currently the Chief Technology officer with Micro Photon Devices, Bolzano, Italy. His main research interests include development of electronics for visible and near-infrared single-photon avalanche diodes for biomedical, quantum sensing and communication applications.

Simone Tisa was born in Milano, Italy, in 1977. He received the M.Sc. (*summa cum laude*) degree in electronics engineering and the Ph.D. degree in electronics from the Politecnico di Milano, Milan, Italy, in 2001 and 2006, respectively. Since 2007, he has been a Senior Engineer with Micro Photon Devices. His research interests include connected with the use of single-photon detectors and active-quenching circuits for ultra-fast imaging applications in astrophysics, and with the design of bidimensional arrays of single-photon avalanche diodes with integrated electronics for the acquisition of time resolved images at single-photon level.

Alexander Flocke studied electrical engineering and the Ph.D. degree with RWTH Aachen University, Aachen, Germany. Since 2008, he has been with iC-Haus where he started in the development department as a Digital Design Engineer. He is currently a Project Manager and digital chip designer with iC-Haus. His main responsibility is the medical business unit of iC-Haus.

Antonio Pifferi is currently a Full Professor of physics with the Department of Physics, Politecnico di Milano, Milan, Italy, and the Director of the Center for Ultrafast Science and Biomedical Optics. His research focuses on the study of photon propagation through diffusive media (diffuse optics) using time-resolved techniques. Diffuse Optics has been explored vertically – from basic research up to exploitation of new application directions – and horizontally – covering diverse applications, including optical mammography, functional brain imaging, food analysis, wood optics.

Paola Taroni was born in Como, Italy, in 1963. She received the graduation degree in nuclear engineering from the Politecnico di Milano, Milan, Italy, in 1987. During 1987–1988, she was a Visiting scientist with G.Harrison Spectroscopy Laboratory, MIT, Cambridge, MA, USA. During 1988–1999, she was a Researcher of the Italian National Council for Research. During 1999–2010, she was an Associate Professor of physics with the Politecnico di Milano. Since 2011, she has been a Full Professor of physics with the Politecnico di Milano. During 2013–2018, she was the Head of the Ph.D. Program in Physics with Politecnico di Milano.

She coauthored about 140 scientific peer reviewed papers and three international patents.

Her research interests include mainly the development of time-resolved optical spectroscopy and imaging, and their applications in biology and medicine, such as the non-invasive characterization of biological tissues, with special interest in time-resolved multi-wavelength optical mammography, non-invasive assessment of breast cancer risk, and therapy monitoring. She is/was a Fellow Member of Optica and SPIE.